

# Resonant Beam Communications

Mingliang Xiong, Qingwen Liu\*, and Mingqing Liu

## Abstract

The sixth generation (6G) mobile communication vision includes the wireless power transfer (WPT) and free-space optical communication (FSO) for the Internet of things (IoT) devices. The laser-based simultaneous wireless information and power transfer (SWIPT) technologies are usually unmovable and have to reduce the power density to meet safety requirements. We propose the resonant beam communications (RBCom) concept which describes a laser-like communication system with the high-power, long-range, high-mobility and human-safe SWIPT ability. The RBCom system is based on the resonant beam charging (RBC) technology, which transfers power via a resonant beam. We investigate both the power transfer and the communication procedures in the RBCom system. The results show that signal-to-noise ratio (SNR)  $> 40$  dB can be obtained, although there is a trade-off between SNR and receiver's power conversion efficiency. RBCom seems to connect the transmitter and the receiver with a invisible fiber. It has the potential to be the enabling technology for the 6G development.

## Index Terms

Resonant Beam Charging, Laser Communications, Optical Wireless Communications, Simultaneous Wireless Information and Power Transfer, Internet of Things.

## I. INTRODUCTION

### A. Motivation

Wireless power transfer (WPT) technologies are becoming increasingly attractive nowadays. These technologies can operate in near field through magnetic fields and electric fields, or far field through radio waves, ultrasonics, infrared waves, visible lights and lasers. With WPT, many Internet of things (IoT) devices can be charged without the constraint of power wires. However, these WPT technologies usually face one or more bottlenecks. Near field WPTs have weak mobility and short range, while some far field WPT technologies are not safe if watt-level power is transferred through the air to a small area like a smart phone.

The resonant beam charging (RBC, also known as distributed laser charging) technology was proposed and investigated recently, which states a safe, high-power, long-range, self-alignment, and high-mobility solution for WPT [1]. The RBC system is similar to a free space external-cavity laser, while in the RBC system the two mirrors are replaced with two retro-reflectors to provide mobility. The power beam resonating between the transmitter and the receiver can be cut off by hands or cloths safely. In the meanwhile, optical communication which adopts light

\* Corresponding author: Qingwen Liu.

M. Xiong, Q. Liu, and M. Liu are with the Department of Computer Science and Technology, Tongji University, Shanghai, Peoples Republic of China, (email: xiongml@tongji.edu.cn, qliu@tongji.edu.cn, clare@tongji.edu.cn).

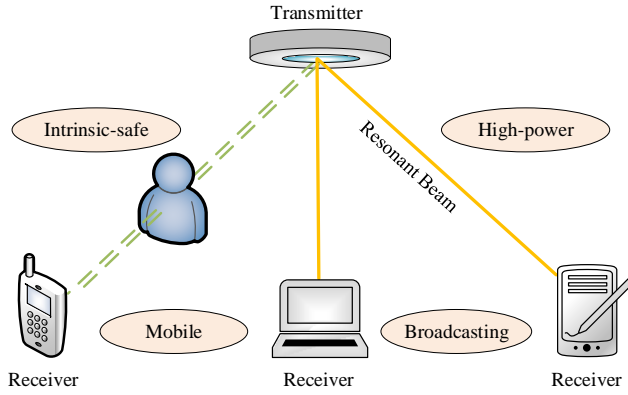


Fig. 1 Simultaneous Charging and Communicating by the RBC System

as the signal carrier to transfer information has made great strides. In this work, we are interested in the potential communication ability in the RBC system. As shown in Fig. 1, there is the possibility to deliver power and data simultaneously to mobile IoT devices via resonant beams.

Klaus David and Hendrik Berndt present the vision of the sixth generation (6G) mobile communication [2]. 6G should move away from wireless radio communication to optical communication and charges mobile devices via radio waves or laser beams, which would be a significant innovation. However, a high-power, high-mobility and human-safe simultaneous information and power transfer (SWIPT) technology is necessary for 6G. The RBC-based SWIPT which possesses the above necessary features can be an enabling technology for the 6G development.

### B. Related Works

The related works are involved in free-space optical communication (FSO), optical wireless power transfer (OWPT), simultaneous optical wireless information and power transfer (OWIPT) and the RBC technologies.

In the past two decades, FSOs which uses medium such as laser, visible light and infrared have been fully investigated. In 1996, Joseph M. Kahn etc. fully summarized the wireless infrared communication model [3]. In 1998, Th. Graf etc. proposed the diode pumped Nd:YAG amplifier laser for intersatellite communication [4]. They reached the 13 dB small signal gain. In 1998, retro-reflectors were used in FSO, which realized the link rate of 460 kbit/s. In 2005, the modelling of corner cubes (retro-reflector) for FSO was presented by Stéphane Junique etc. and showed that the field of view can be more than ten-fold of that of the modulator [5]. In 2007, the cat's eye (retro-reflector) optics arrangement was used in FSO [6]. The eye-safe issue in laser FSO was introduced in [7]. In 2013, Toshihiko Komine etc. made the fundamental analysis for visible light communication (VLC) and stated the possibility of 10 Gb/s data rate with white light-emitting diodes (LEDs) [8]. In 2013, Dobroslav Tsonev etc. achieved the 3 Gb/s orthogonal frequency division multiplexing(OFDM)-based VLC with a single LED [9].

Most OWPT technologies are based on laser. In 2011, Aakash Sahai etc. proposed the OWPT with long wavelength (greater than 1400 nm) laser diodes (LDs) which have higher power density threshold for human safety [10]. In 2012, J Mukherjee etc. developed the high-efficiency laser power converters (LPCs) for OWPT and

obtained the experimental conversion efficiency of 44.6% [11]. In 2013, Sung-Man Kim etc. adopted beamforming with a spatial light modulator and a white LED, and achieved the transmission efficiency of 1.3% [12]. In 2014, Weiyang Zhou and Ke Jin evaluated the efficiency of LD in different driving modes (the continuous mode and the pulse mode) for OWPT [13]. In 2017, vertical multi junction (VMJ) solar cells are used for long distance OWPT and obtained the optical-to-electrical conversion efficiency of 49.83% [14]. The same year, Vikram Iyer etc. used the retro-reflector in laser-based OWPT to create guard beams, and verified the safety for a human moving at a maximum speed of 44 m/s when charging a smart phone with electrical power of 2 W [15]. In 2018, the coupled model on energy conversion with laser-based OWPT was investigated [16]; and vertical-cavity surface-emitting lasers (VCSELs) with the features of small size, high output power and high efficiency were investigated [17]. Recently in 2018, Ke Jin and Weiyang Zhou made a technique review on the laser power transmission [18].

In 2015, John Fakidis etc. designed the FSO link for small cell backhaul communication and power supply, and achieved the link efficiency of 0.74% and harvested power of 10.4 mW at the distance of 5.2 m [19]. The same year, Won-Ho Shin etc. used the self-reverse-biased solar panel receiver circuit for the communication and energy harvesting, achieving the data rate of 17.05 Mbps and the bit error rate of  $1.1 \times 10^{-3}$ . In 2017, the PV efficiency of 50% is achieved in OWIPT at a single wavelength of operation [20]. In 2018, John Fakidis etc. obtained 0.5 Gb/s data rate using OFDM and 42% PV efficiency [21].

In 2016, Qingwen Liu etc. reported the distributed laser charging (DLC), which is capable of charging mobile devices via resonant beams [1]. Afterwards, Qingqing Zhang etc. analysed the transmission model of the DLC system, and then, proposed the adaptive RBC (ARBC) system to improve the energy utilization [22, 23]. In 2018, Wen Fang etc. proposed the fair scheduling algorithm in RBC system [24]. Mingliang Xiong etc. proposed the time-division multiple access (TDMA) design in the RBC system to enable the multi-user charging control [25].

### C. Our Contribution

We at first propose the resonant beam communications (RBCom) system, which is a RBC-based OWIPT system. We present the analytical model of the RBCom system theoretically to describe the significant progresses of the information and power transfer. In the analytical model, we consider the impacts on the output power and the transmission efficiency, prove the feasibility of modulating a signal on the resonant beam, and investigate the noise source and the communication performance. The numerical results show a good communication performance.

The remainder of the paper is as follows. The background, including the components of the RBCom system and its mechanism, is introduced in Section II. The analytical models of power transfer and information transfer are presented in Section III. The numerical results and the discussion are presented in Section IV. Finally, a conclusion is made in Section V.

## II. SYSTEM DESCRIPTION

The resonant beam charging (RBC) system can transfer wireless power from the transmitter to the receiver via a resonant beam. Fig. 2 shows the components and structure of the RBC system. The RBC system comprises a current regulator, a diode pump, a gain medium, two retro-reflectors R1 and R2, and a photovoltaic (PV) panel.

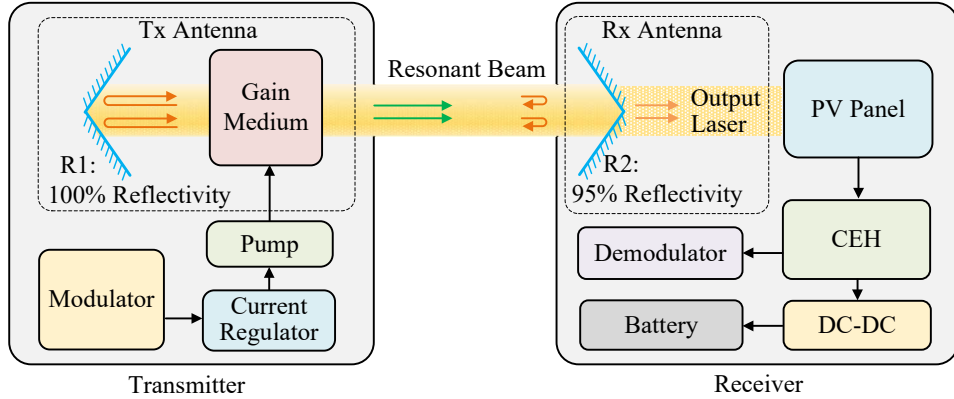


Fig. 2 Resonant Beam Communication (RBCom) System

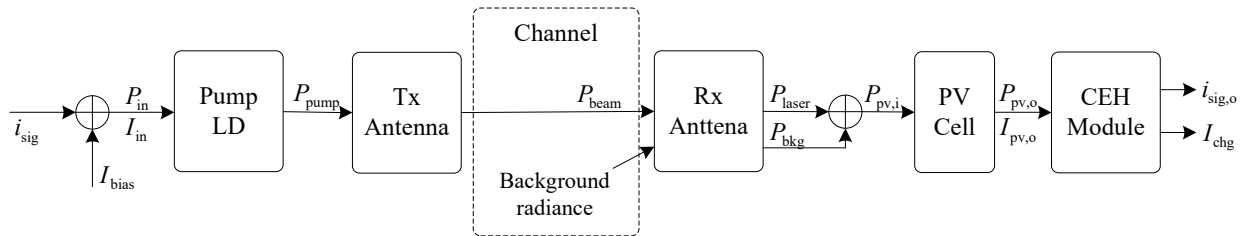


Fig. 3 Analytical Model for RBCom System

The RBC structure is similar to a laser cavity. In a general laser cavity, R1 and R2 are mirrors. The beam resonates between the two mirrors, while stimulating the gain medium for more photons. In the RBC structure, R1 and R2 are retro-reflectors which can reflect the incident beam from any directions within the field of view (FOV) to the reverse orientation [5]. Therefore, the RBC transmitter and the receiver can move flexibly while keeping the beam shuttling between the two retro-reflectors. As a retro-reflector with partial reflection, R2 allows parts of the photons passing through to form a laser beam. At last, the PV panel converts the coupled output laser into electricity for charging batteries. There are several features with respect to the RBC system, including long-range, movable, high-power, and intrinsic safe.

In the RBC system, the current regulator is adopted to provide electricity for the pump. The pump can be a laser diode (LD) or a vertical cavity surface emitting laser (VCSEL). The gain medium absorbs the energy from the pump laser beam to maintain the resonance of the intra-cavity beam. In the receiver, a direct current to direct current (DC-DC) converter is adopted to adjust the charge voltage/current of the battery, or to keep the PV panel working in the maximum power point the normal charge voltage/current can't be maintained.

We propose the resonant beam communication (RBCom) system based on the RBC structure to realize simultaneous wireless information and power transfer (SWIPT). The information can be modulated on the resonant beam, so that an invisible straight link for data and power can be created. It is possible to enable future IoT applications which is critical for wireless power and communication performance.

As shown in Fig. 2, the RBCCom structure based on the RBC system contains the pump, the transmitting (Tx) antenna, the receiving (Rx) antenna, and the PV panel. These basic components are employed to transfer power. For data transmission, the system integrates a modulator, a linear current regulator and a processing module for communication and energy harvesting (CEH) [26]. The current regulator generates current according to the modulated signal to drive the pump. With the modulated input current, the resonant beam as well as the output laser carry not only the power but also the information. The CEH module receives the variant output current from the PV panel, then, it separates the signal to the communication branch and guide the energy to the energy harvesting branch. The next section will analyse the procedures of transferring power and data via a resonant beam simultaneously.

### III. ANALYTICAL MODEL

For analysis, we describe the RBCCom system in Fig. 3. The pump input current  $I_{\text{in}} = I_{\text{bias}} + i_{\text{sig}}$  generated by the current regulator comprises the signal current  $i_{\text{sig}}$  and the bias current  $I_{\text{bias}}$ . We notate the input power of the pump LD as  $P_{\text{in}}$ , notate the pump laser power as  $P_{\text{pump}}$ , notate the resonant beam power as  $P_{\text{beam}}$ , and notate the coupled output laser from the Rx antenna as  $P_{\text{laser}}$ . The power of the background light is  $P_{\text{bkg}}$ . The power and current output from the PV panel are  $P_{\text{pv}}$  and  $I_{\text{pv}}$ . At last, the CEH module separate the  $I_{\text{pv}}$  into the signal current  $i_{\text{sig},o}$  for communication and the charge current  $I_{\text{chg}}$  for energy harvesting. The subsections bellow analyse the power transfer and data transfer processes detailedly.

#### A. Power Transfer

The WPT process in the RBCCom system includes 3 stages: 1) the input power  $P_{\text{in}}$  to the pump laser power  $P_{\text{pump}}$  by the pump LD; 2) the power transmission between the Tx and Rx antennas, after which  $P_{\text{pump}}$  changes to  $P_{\text{beam}}$  and then to the coupled output power  $P_{\text{laser}}$ ; and, 3)  $P_{\text{laser}}$  to the output power of the PV panel  $P_{\text{pv}}$ . We analyse the above stages to depict the WPT in the RBCCom system. We find the linear relationship between the input and the output power after analysis, which enables the distortionless signal modulation and transmission in the RBCCom structure.

1) *Pump LD*: The pump LD generates a laser beam to stimulate and drive the gain medium. The current-power (I-P) characteristics of the pump LD can be described as [27]:

$$P_{\text{pump}}(I_{\text{in}}) = \frac{hc}{q\lambda} \eta_{\text{S}} [I_{\text{in}} - I_{\text{th}}], \quad (1)$$

and

$$\eta_{\text{S}} = \eta_{\text{inj}} \frac{\gamma_{\text{out}}}{\gamma_{\text{c}}}, \quad (2)$$

where  $h$  is Planck's constant,  $c$  is the speed of light in vacuum,  $q$  is the electron charge,  $\lambda$  is the emission wavelength, and  $I_{\text{th}}$  is the constant threshold current.  $\eta_{\text{inj}}$  and  $I_{\text{th}}$  are temperature dependent.  $\gamma_{\text{out}}$  and  $\gamma_{\text{c}}$  are determined by the parameter of the LD. Fig. 4 shows the I-P characteristic curve of the pump LD. We can find that the relationship between the pump laser power and the input current is close to linearity after the input current exceeding the threshold.

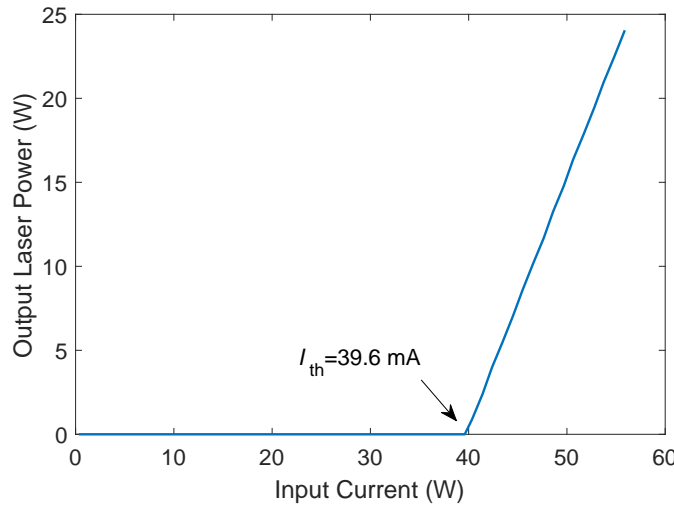


Fig. 4 Pump LD: Output Power vs. Input Current

2) *Coupled Output Laser*: The laser generation mechanism between the Tx and Rx antennas are similar to that of a LD pumped solid state laser. For reason of simplicity, the RBCom system consisting of the two antennas can be modelled as a long-cavity solid state laser. As analysed by [28], the output laser power from the Rx antenna can be described as:

$$P_{\text{laser}} = \eta_{\text{store}} P_{\text{pump}} f(d) + C, \quad (3)$$

where  $f(d)$  is the function related to the distance  $d$  between the two antennas,  $C$  is a constant value depending on the internal parameters, and  $\eta_{\text{store}}$  is the conversion efficiency of population inversion. The gain medium absorbs the power from the incident pump laser to realize the population inversion, which is a necessary step for generating the laser beam. The function  $f(d)$  can be described as [28]:

$$f(d) = \frac{2(1-R)m}{(1+R)e^{-2\pi \cdot \frac{a^2}{\lambda d}} - (1+R)\ln R}, \quad (4)$$

where  $R$  is the reflectivity of R2,  $m$  is the overlap efficiency, and  $a$  is the radius of the aperture that the beam passes through. In summary, the above process provide a linear relationship between  $P_{\text{laser}}$  and  $P_{\text{pump}}$  at specified  $\lambda$  and  $d$ .

3) *PV Panel*: The PV panel converts the coupled output laser into electrical power. Fig. 5 is the equivalent circuit of a PV panel [29, 30]. An ideal PV panel can be modelled as a photo-current source  $I_{\text{ph}}$  connected in parallel to a diode. In Fig. 5,  $I_d$  is the forward current of the diode. In reality, the PV panel model should add a shunt resistor  $R_{\text{sh}}$  and a series resistor  $R_s$ . Therefore, according to Kirchhoff's law, the current-voltage (I-V) characteristics of a PV panel can be described as [29, 30]:

$$I_{\text{pv},o} = I_{\text{ph}} - I_d - \frac{V_{\text{pv},o} + I_{\text{pv},o}R_s}{R_{\text{sh}}}, \quad (5)$$

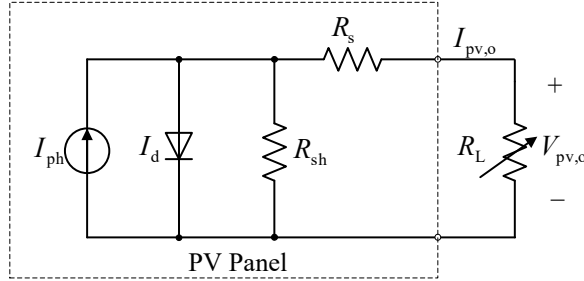


Fig. 5 PV Panel Equivalent Circuit

and

$$\begin{aligned} I_d &= I_0 \left( e^{\frac{V_d}{n_s n V_T}} - 1 \right) \\ &= I_0 \left( e^{\frac{V_{pv,o} + I_{pv,o} R_s}{n_s n V_T}} - 1 \right), \end{aligned} \quad (6)$$

where  $I_0$  is the reverse saturation current, and  $n_s$  is the number of cells connected in series in the PV panel. For single PV cell,  $n_s = 1$ .  $V_T$  is the junction thermal voltage of the diode that related to the temperature:

$$V_T = \frac{kT}{q}, \quad (7)$$

where  $n$  is the diode ideality factor,  $k$  is the Boltzmann's constant, and  $T$  is the panel's temperature in Kelvin.

The photocurrent  $I_{ph}$  is related to the irradiance of the input light and can be estimated by [31]:

$$I_{ph} = \frac{G}{G_{STC}} \cdot I_{ph,STC}, \quad (8)$$

where  $G$  is the input irradiance in  $\text{W/m}^2$ ,  $G_{STC}$  is the standard-test-condition (STC) irradiance  $1000 \text{ W/m}^2$ , and  $I_{ph,STC}$  is the photocurrent at  $G_{STC}$ . The STC cell temperature  $25^\circ\text{C}$ . For a given irradiated area  $A_{rcv}$  and input light power  $P_{pv,i}$ , the input irradiance level can be obtained as:

$$G = \frac{P_{pv,i}}{A_{rcv}}. \quad (9)$$

The optical-to-electrical conversion responsivity in  $\text{A/W}$  can be defined as:

$$\rho = \frac{I_{ph,STC}}{A_{rcv} G_{STC}}. \quad (10)$$

Therefore, the photocurrent in (8) can be rewritten as [3, 19]:

$$I_{ph} = \rho P_{pv,i}. \quad (11)$$

From (11), we can prove the linear relationship between the photocurrent and the input light power.

Fig. 6 shows the I-V characteristic curves at different light power. The PV panel operates at different voltage with different load resistance  $R_L$  although the light power is at the same level. We can find a linear region in which the PV panel works close to a constant-current source regardless of the load resistance  $R_L$ . In the linear region, for each given  $P_{pv,i}$  the output current,  $I_{pv,o}$ , of the PV decreases very slowly with the increasing of output voltage, i.e.,  $I_{pv,o}$  is almost equal to  $I_{ph}$ . The load circuit is generally modelled as an adjustable resistor. Therefore,

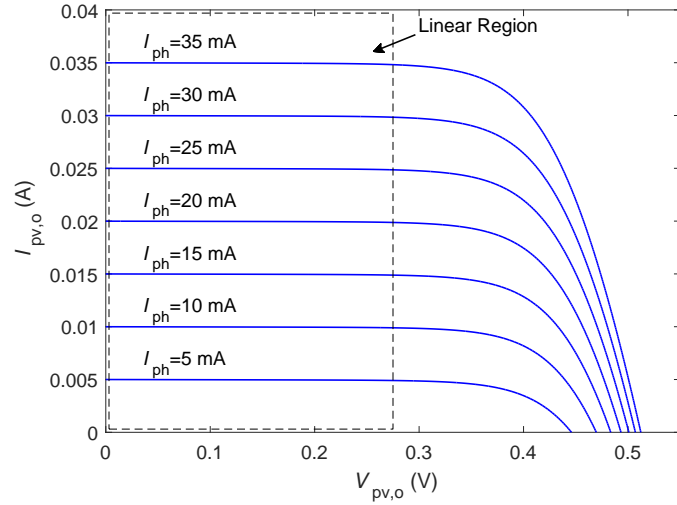


Fig. 6 I-V Characteristics of PV Panel

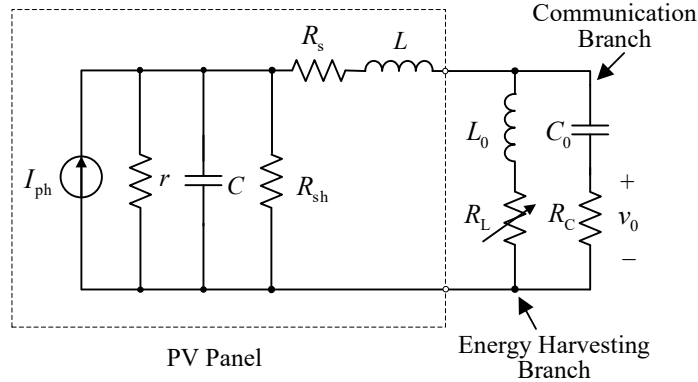


Fig. 7 Communication and Energy Harvesting (CEH) Alternating Current Equivalent Circuit

it is possible to adjust the load resistance to keep the operating point of the PV panel in its linear region. Note that increasing the series resistance  $R_s$  will decrease the linear region area. Also, a large shunt resistance  $R_{sh}$  will destroy the constant-current property in the linear region [29]. It is recommended to reduce  $R_s$  and  $R_{sh}$  in experiments or productions.

### B. Information Transfer

In the subsection above, we analyse the power transfer process of the RBCom system. If the alternating current (AC) signal is small and the temperature shifting is slow,  $\eta_s$  can be assumed as a constant. Moreover, the value of  $f(d)$  at a specific distance  $d$  can be considered as a constant attenuation  $\eta_d$ . From (1), (3) and (11), the output current of the PV panel in the linear region can be described as:

$$\begin{aligned} I_{pv,o} \approx I_{ph} &= \rho \left\{ \eta_{store} \eta_d \left\{ \frac{hc}{e\lambda} \eta_s [I_{in} - I_{th}] \right\} + C \right\} \\ &= \gamma [I_{in} - I_{th}] + \beta, \end{aligned} \quad (12)$$

where

$$\gamma = \rho \eta_{\text{store}} \eta_d \eta_s \frac{hc}{e\lambda}, \text{ and } \beta = \rho C. \quad (13)$$

From (12),  $\gamma$  is a constant factor, which verifies the linear modulation ability of the RBCCom system.

At the receiver, the PV panel connects to the CEH module which consists of the communication branch and the energy harvesting branch [26]. In the following, we present the modulation model, the transmission loss, the AC equivalent circuit and the noise impacts of the communication.

1) *Modulation*: As analysed above, the input current  $I_{\text{in}}$  can be modulated to transfer information. The signal current by on-off keying (OOK) modulation can be described as:

$$i_{\text{sig}} = k(t) I_m \cos(\omega_0 t + \phi), \quad k(t) \in \{0, 1\}, \quad (14)$$

where  $k(t)$  represents the data in binary,  $I_m$  is the carrier amplitude,  $\omega_0$  is the carrier frequency in rad/s, and  $\phi$  is the carrier phase. In the RBCCom system, the modulated signal is hold up by a bias current  $I_{\text{bias}}$ . Therefore the input current of the pump LD can be described as:

$$\begin{aligned} I_{\text{in}} &= I_{\text{bias}} + i_{\text{sig}} \\ &= I_{\text{bias}} + k(t) I_m \cos(\omega_0 t + \phi). \end{aligned} \quad (15)$$

Note that  $I_{\text{in}}$  is the combination of a direct current (DC) part  $I_{\text{bias}}$  and an AC part  $i_{\text{sig}}$ . It is necessary to adopt a bias current as the LD's input current must excess the threshold. Moreover, the bias current provides the primary charging power for the receiver. We define the modulation depth  $m$  to describe the scale of the modulated signal. Therefore, we have the following definition of the signal amplitude:

$$I_m = m(I_{\text{bias}} - I_{\text{th}}), \quad 0 < m \leq 1. \quad (16)$$

The permitted range of  $m$  constraint the signal amplitude, so that the modulated signal will always excess the threshold.

2) *Transmission Loss*: (4) illustrates the transmission loss varying the distance between the transmitter and the receiver in the RBCCom system, which is distinct from that of the general laser-based communication system [28, 32]. The power loss is related to the parameters of the components in the RBCCom system, such as the radius of the aperture and the overlap efficiency. Besides the distance, the atmosphere condition between the Tx antenna and the Rx antenna effects the resonant beam transmission. The resonant beam is usually at infrared wavelength. Therefore, the refractive turbulence and the water vapor in the atmosphere can result in attenuation of the beam power [7]. Particles such as smoke and fog whose size is larger than the wavelength can cause the power loss [33]. Therefore, it is important to choose the appropriate wavelength to reduce the power loss in experiments or productions.

3) *Receiver's AC Equivalent Circuit*: Fig. 7 depicts the equivalent circuit of the PV panel and CEH module for the AC signal transmission. The the AC part  $i_{\text{sig}}$ , is coupled by the capacitor  $C_0$  and transmitted to the communication branch. The energy harvesting branch receives the DC part and chokes the AC part by the inductor  $L_0$ . The operating point is determined by the DC part and the load resistance. For analysing the AC signal transmission, the diode in Fig. 5 can be replaced with the small-signal dynamic resistance  $r$  and the cell capacitance  $C$  in parallel, where

$C = C_T + C_d$  is the total capacitance of the transition capacitance  $C_T$  and the diffusion capacitance  $C_d$  in parallel. The quantities  $r$ ,  $C_T$ , and  $C_d$  are the dynamic parameters of PV panels. The inductor  $L$  models the inductance of wires connected to the PV panel.

The transition capacitance can be determined by the following equation [34]:

$$C_T = \frac{B}{\sqrt{V_0 - V_d}} = A \sqrt{\frac{e\epsilon_0 N_B}{2(V_0 - V_d)}}, \quad (17)$$

where  $A$  is the area of the PV panel,  $\epsilon$  is the permittivity of the semiconductor material (Si:  $\epsilon = 11.7$ , GaAs:  $\epsilon = 13.1$ ),  $\epsilon_0 = 8.85 \times 10^{-12}$  is the vacuum permittivity,  $N_B$  is the doping concentration in the base region.  $V_0$  is the built-in voltage related to the temperature and the doping concentration of the semiconductor [35].  $V_d$  is the applied voltage at the diode. Therefore, it can be learned that  $C_T$  is a voltage dependent parameter.

The diffusion capacitance can be determined by the following equation [34, 36]:

$$C_d = \frac{\tau}{2nV_T} I_0 e^{\frac{V_d}{nV_T}}, \text{ for } \omega\tau \ll 1, \quad (18)$$

where  $\omega$  is the angular frequency of the signal, and  $\tau$  is the minority carrier lifetime which is temperature dependent and can be measured in experiments [37].

The small-signal dynamic resistance  $r$  can be determined by the following equation [38]:

$$\frac{1}{r} = \frac{dI_d}{dV_d} = \frac{1}{nV_T} I_0 e^{\frac{V_d}{nV_T}}. \quad (19)$$

Therefore,  $r$  is voltage dependent. If  $I_d \gg I_0$ , (19) can be rewritten as:  $r = V_T/I_d$ .

4) *Received Signal:* From (12) and (14), the AC part of the photocurrent can be obtained as:

$$i_{\text{ph,sig}} = \gamma k(t) I_m \cos(\omega_0 t + \phi). \quad (20)$$

The frequency response of the PV-CEH network, which has the input of the photocurrent and the output of the signal voltage on the resistor  $R_C$ , can be evaluated as [26]:

$$\begin{aligned} |h_{\text{ph}}(\omega)|^2 &= \left| \frac{v_o(\omega)}{i_{\text{ph}}(\omega)} \right|^2 \\ &= \left| \frac{\frac{R_{LC}}{R_s + j\omega L + R_{LC}} \frac{R_C}{\frac{1}{j\omega C_0} + R_C}}{\frac{1}{r} + \frac{1}{\frac{1}{j\omega C}} + \frac{1}{R_{sh}} + \frac{1}{R_s + j\omega L + R_{LC}}} \right|^2, \end{aligned} \quad (21)$$

where  $\omega$  is the angular frequency,  $j = \sqrt{-1}$  and  $R_{LC}$  is the resistance of the parallel network of the energy harvesting branch and the communication branch, which is formulated detailedly in [26]. Therefore, the average signal power output from the resistor  $R_C$  can be calculated as:

$$S_o = |h_{\text{ph}}(\omega_0)|^2 \overline{i_{\text{ph,sig}}^2}, \quad (22)$$

where  $\overline{i_{\text{ph,sig}}^2}$  is the average photocurrent of the carrier signal. If the operating point lies in the linear region, we can obtain:

$$\overline{i_{\text{ph,sig}}^2} = \frac{(\gamma I_m)^2}{2} = \frac{[\gamma m(I_{\text{bias}} - I_{\text{th}})]^2}{2}. \quad (23)$$

5) *Receiver Noise*: The effective noise at the receiver includes the background radiance induced noise, the photo-current shot noise, and the thermal noise of the circuit, which are analysed respectively below. [26, 39].

The background radiance in the environment comes from the sunlight or the lamplight. The light power of the background radiance received by the PV panel can be formulated as [39]:

$$P_{\text{bkg}} = \eta_{\text{RX}} H_{\text{bkg}} B_{\text{IF}} A_{\text{RX}} \Phi_{\text{rcv}} \Gamma, \quad (24)$$

where  $\eta_{\text{RX}}$  is the optical efficiency of the RX antenna,  $H_{\text{bkg}}$  is the background radiance in  $\text{W} \cdot \text{m}^{-2} \cdot \text{nm}^{-1} \cdot \text{sr}^{-1}$ ,  $B_{\text{IF}}$  is the optical bandwidth of the filter installed behind R2.  $A_{\text{RX}}$  is the receiving area of the RX antenna, and  $\Phi_{\text{rcv}}$  is the PV panel's solid angle field of view. The background radiance in the RBCOM system should pass through the mirror R2 which has a low transmittance  $\Gamma$ . Therefore an additional attenuation on the background irradiance exists, which can't happen in the general laser-based communication system or visible light communication (VLC) system. From (11), the photo current caused by the background irradiance can be calculated as:

$$i_{\text{ph,bkg}} = \rho P_{\text{bkg}}. \quad (25)$$

The shot noise comes from the optical-to-electrical process in the PV panel and can be modelled by a Gaussian distribution which has a flat power spectral density (PSD) [40]. The one-side PSD of the shot noise expressed in  $\text{A}^2/\text{Hz}$  can be calculated as [3]:

$$N_{\text{pv,Hz}^{-1}}^{\text{sh}} = 2e\rho P_{\text{pv,i}}, \quad (26)$$

where  $e$  is the electron charge,  $\rho$  is the optical-to-electrical efficiency described in (11), and  $P_{\text{pv,i}}$  is the average optical power over the PV panel including the laser power  $P_{\text{laser}}$  and the background irradiance power  $P_{\text{bkg}}$ . The shot noise current experiences the same network, i.e. the same frequency gain, with the signal. Therefore, the one-side PSD of the output from the contribution of the shot noise can be calculated as:

$$N_{\text{o}}^{\text{sh}}(\omega) = |h_{\text{ph}}(\omega)|^2 \times 2e\rho(P_{\text{laser}} + P_{\text{bkg}}). \quad (27)$$

The thermal noises are generated by the resistor in the equivalent circuit depicted in Fig. 7. The one-side PSD of the thermal noise generated by the resistor  $R_{\text{C}}$  can be calculated as [3]:

$$N_{\text{o,R}_C}^{\text{th}} = 4kT R_{\text{C}}, \quad (28)$$

where  $k$  is Boltzmann's constant,  $T$  is the temperature of  $R_{\text{C}}$  in Kelvin. Likewise, the one-side PSD of the output contributed by all the thermal noises in the circuit can be calculated as [26]:

$$\begin{aligned} N_{\text{o}}^{\text{th}}(\omega) = & |h_{\text{R}_C}(\omega)|^2 N_{\text{o,R}_C}^{\text{th}} + |h_{\text{sh}}(\omega)|^2 N_{\text{o,sh}}^{\text{th}} \\ & + |h_{\text{R}_L}(\omega)|^2 N_{\text{o,R}_L}^{\text{th}} + |h_r(\omega)|^2 N_{\text{o,r}}^{\text{th}} \\ & + |h_{\text{R}_s}(\omega)|^2 N_{\text{o,R}_s}^{\text{th}}, \end{aligned} \quad (29)$$

where  $N_{\text{o,sh}}^{\text{th}}$ ,  $N_{\text{o,R}_L}^{\text{th}}$ ,  $N_{\text{o,r}}^{\text{th}}$  and  $N_{\text{o,R}_s}^{\text{th}}$  are the one-side PSD of the thermal noise that the resistors  $R_{\text{sh}}$ ,  $R_{\text{L}}$ ,  $r$  and  $R_{\text{s}}$  respectively generates, and  $|h_{\text{R}_C}(\omega)|^2$ ,  $|h_{\text{sh}}(\omega)|^2$ ,  $|h_{\text{R}_L}(\omega)|^2$ ,  $|h_r(\omega)|^2$  and  $|h_{\text{R}_s}(\omega)|^2$  are the frequency response of the networks that the thermal noises from  $R_{\text{C}}$ ,  $R_{\text{sh}}$ ,  $R_{\text{L}}$ ,  $r$  and  $R_{\text{s}}$  respectively experiences.

TABLE I Parameters Definition

Quantity	Symbol	Value	Unit
Reverse saturation current	$I_0$	$9.381 \times 10^{-9}$	A
Diode ideality factor	$n$	1.318	-
Temperature	$T$	298.15	K
Series resistance	$R_s$	1.3	$\Omega$
Shunt resistance	$R_{sh}$	5000	$\Omega$
Number of PV cells	$n_s$	1	-
optical-to-electrical resposivity	$\rho$	0.746	A/W
Dynamic resistance	$r$	240	$\Omega$
Cell capacitance	$C$	$3.8 \times 10^{-5}$	nF
Wire inductance	$L$	120	nH
AC chock inductor	$L_0$	10	mH
AC coupling capacitor	$C_0$	0.1	$\mu\text{F}$
Optical efficiency of Rx antenna	$\eta_{RX}$	0.9	-
Background irradiance	$H_{bkg}$	0.2	$\text{W}\cdot\text{m}^{-2}\cdot\text{nm}^{-1}\cdot\text{sr}^{-1}$
Bandwidth of optical filter	$B_{IF}$	20	nm
Area of Rx antenna	$A_{RX}$	1	$\text{cm}^2$
Solid angle of view of PV	$\Phi_{rcv}$	$2\pi(1 - \cos 30^\circ)$	sr
Transmittance of mirror R2	$\Gamma$	0.05	-
Average received laser power	$P_{laser}$	0.05	W
Peak-to-peak swing of received laser power	$P_{laser,pp}$	0.001	W
Bandwidth of signal filter	$BW$	50	MHz
Communication resistor	$R_C$	10	$\Omega$
Load resistance	$R_L$	10	$\Omega$

6) *Signal-to-Noise Ratio:* Above all, the signal-to-noise ratio (SNR) can be obtained as:

$$\text{SNR} = \frac{S_o}{\int_0^{\text{BW}} [N_o^{\text{sh}}(\omega) + N_o^{\text{th}}(\omega)] d\omega}, \quad (30)$$

where BW is the bandwidth of the lowpass filter at the output port.

#### IV. RESULT AND DISCUSSION

In this section, we investigate the performance of the receiver. We at first introduce the parameters used in the simulation. Then we discuss the variation in system features with different selections of operating points. We also depict the network frequency response for each signal or noise sources. At last, we illustrate the power conversion efficiency and the SNR at different operating point, and discuss the trade-off on the selection of the operating point.

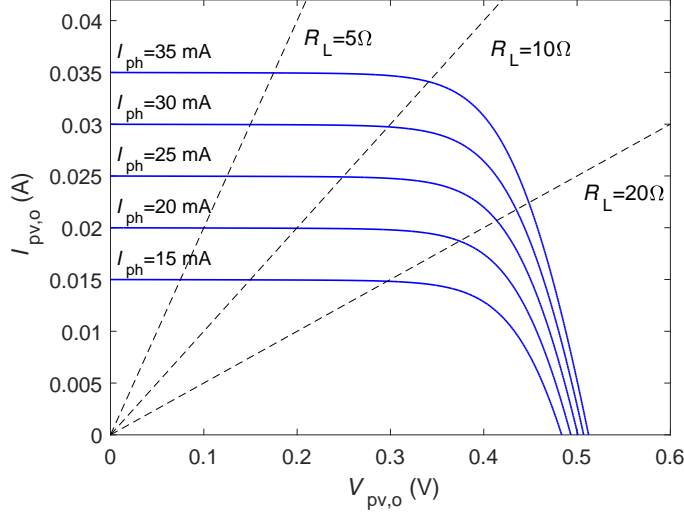


Fig. 8 Operating Points at Different  $I_{\text{ph}}$  and  $R_L$

#### A. Parameters

The following simulation is with the parameters listed in Table I by default, unless otherwise specified. For reasons of simplicity, we use the single cell PV panel, i.e.  $n_s = 1$ , also the receiving area is assumed as  $1 \text{ cm}^2$ . The I-V characteristic curve and the capacitance voltage (C-V) characteristic curve are obtained from [41]. The parameters of the PV cell  $I_0, n, T, R_s, R_{\text{sh}}$  are obtained by using the curve fitting tool in MATLAB, i.e., to search the optimal values of the five parameters to make the model expressed by (5) very close to the I-V curve. As is analysed in [42], the maximum optical-to-electrical conversion efficiency of a mono Si PV cell can reach about 25% under STC. Assuming the PV panel efficiency of 25%, we obtained the conversion responsivity  $\rho$  as 746 mA/W. The wire inductance  $L$  is obtained from [26]. The parameters of background irradiance  $H_{\text{bkg}}$  are obtained from [39]. The average received laser power  $P_{\text{laser}}$  is assumed as 0.05 W, then, the DC part of the photocurrent  $I_{\text{ph,dc}}$  can be obtained as 37.3 mA. The peak-to-peak swing of the received laser power  $P_{\text{laser,pp}}$  is assumed as 0.001 W. Then, the AC part of the photocurrent  $I_{\text{ph,ac}}$  can be obtained as 0.746 mA.

#### B. Operating Point

Fig. 8 depicted the I-V curves of the PV panel when the photocurrent  $I_{\text{ph}} = \{0.015 \text{ W}, 0.02 \text{ W}, 0.025 \text{ W}, 0.03 \text{ W}, 0.035 \text{ W}\}$ . The dashed line represents the load resistance at  $R_L = \{5 \Omega, 10 \Omega, 20 \Omega\}$ . The intersection point of one I-V curve and one  $R_L$  line indicates the operating point. We can find that with a fixed  $R_L$ , the operating point varies with  $I_{\text{ph}}$ .

A more intuitive illustration is shown in Fig. 9. Given a certain  $R_L$ , the relationship between the PV output current  $I_{\text{pv,o}}$  and the photocurrent  $I_{\text{ph}}$  is obtained. Each curve has a two linear segments, between which a bent segment connects them. If the operating point lies in the bent segment, a high-power (large peak-to-peak current of  $I_{\text{ph}}$ ) signal will face with heavy distortion, as  $I_{\text{pv,o}}$  varies with  $I_{\text{ph}}$  nonlinearly. However, in the right segment

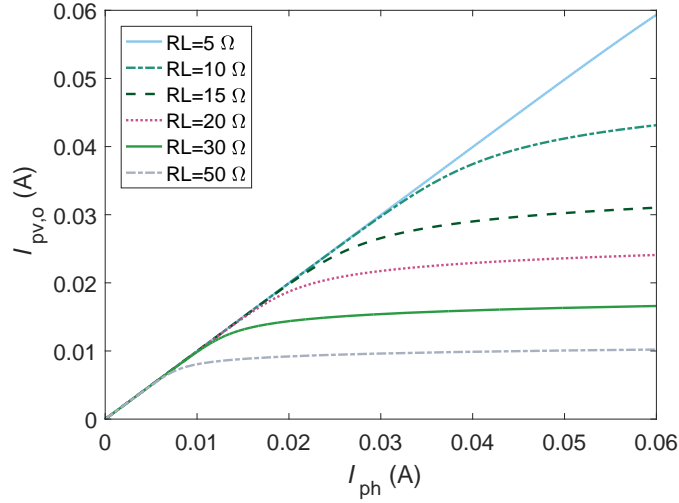


Fig. 9 Relationship Between  $I_{pv,o}$  and  $I_{ph}$

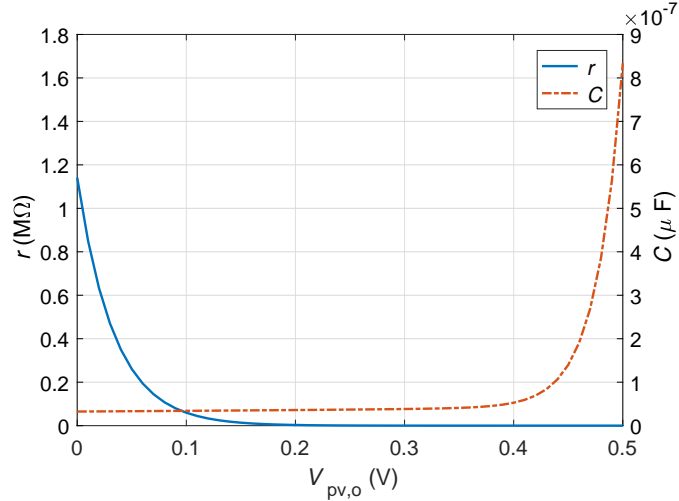


Fig. 10 Dynamic Resistance and Cell Capacitance vs. Cell Voltage

region,  $I_{pv,o}$  changes slightly with the variation of  $I_{ph}$ , that means the amplitude of the output signal will be heavily reduced.

Fig. 10 illustrates the variation in the dynamic resistance  $r$  and the cell capacitance with the cell voltage  $V_{pv,o}$ . With a low cell voltage,  $r$  in  $M\Omega$  level is much large. However,  $r$  decreases to several  $\Omega$  at a high voltage. On the contrary,  $C$  is in a low level and increases rapidly when  $V_{pv,o}$  grows. From this figure, we can conclude that a low cell voltage is helpful for communication as the large dynamic resistance will improve the signal gain of the network. Furthermore, at the low-voltage operating point, the cell capacitance is low, which increases the parallel impedance for high-frequency signals. As a result, the signal will obtain a large gain in the network.

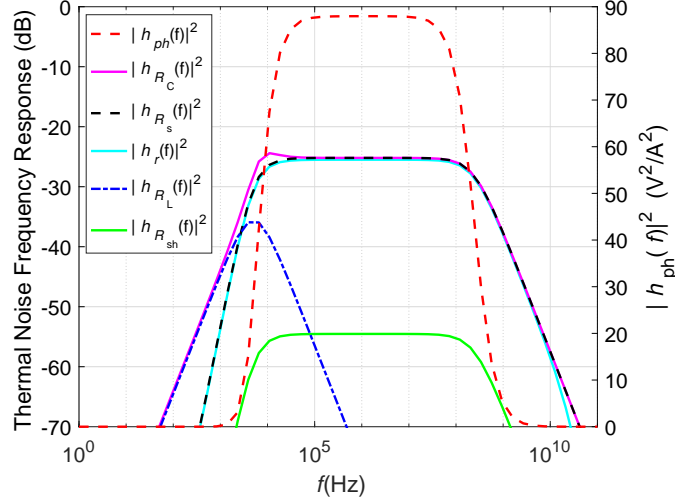


Fig. 11 Network Frequency Response

### C. Frequency Response

In the receiver, there are data signal, shot noise and five thermal noises affecting the output voltage on the communication resistor  $R_C$ . The frequency response,  $|h_{ph}(\omega)|^2$ , of the network at the default operating point specified by Table I is depicted in Fig. 11, which illustrates the network transmission pattern from the input  $I_{ph}$  to the output  $v_o$ . This network is a bandpass filter, which reaches a high flat gain between 100 kHz and 10 MHz. The data signal and the shot noise passing through this network share the same gain. The other five curves in Fig. 11 are the frequency response of the network for the thermal noises. The most effective noises are from  $R_C$ ,  $R_s$  and  $r$ . The thermal noise generated by  $r$  only have effects on low frequency signals. Note that, the frequency response illustrate above is under the condition of default operating point. Other operating point may lead to different features.

The SNR at the receiver is also a function of the carrier frequency. We assume the output voltage of the communication branch  $v_o$  will pass through a lowpass filter whose bandwidth BW is assumed as 1 GHz. Under this condition, the variation in SNR with the carrier frequency is depicted in Fig. 12. The figure plots out three SNR curves under the conditions where the communication resistor  $R_C = \{10 \Omega, 100 \Omega, 500 \Omega\}$ . The result shows that there is a flat region x the middle frequency, where the SNR is almost a constant value. The SNR is greater than 40 dB in this region. Outside the flat region, the SNR decreases sharply. Therefore, a proper selection of the carrier frequency will provide an optimal channel capacity. In the flat region, the greater  $R_C$  leads to the lower SNR. However, increasing  $R_C$  will expand the flat region.

### D. Trade-off on Power Efficiency

At different operating point, the receiver will reach different power conversion efficiency and SNR. Fig. 13 shows the power conversion efficiency  $\eta_{pv}$  and SNR vary with different provided  $I_{ph}$ . Three types of lines indicate the different load resistance  $R_L = \{10 \Omega, 15 \Omega, 20 \Omega\}$ . Result shows that  $\eta_{pv}$  has a maximum point in the middle range of  $I_{ph}$ . The SNR will decrease with the increment of  $I_{ph}$ . The larger  $R_L$  results in the smaller SNR. The

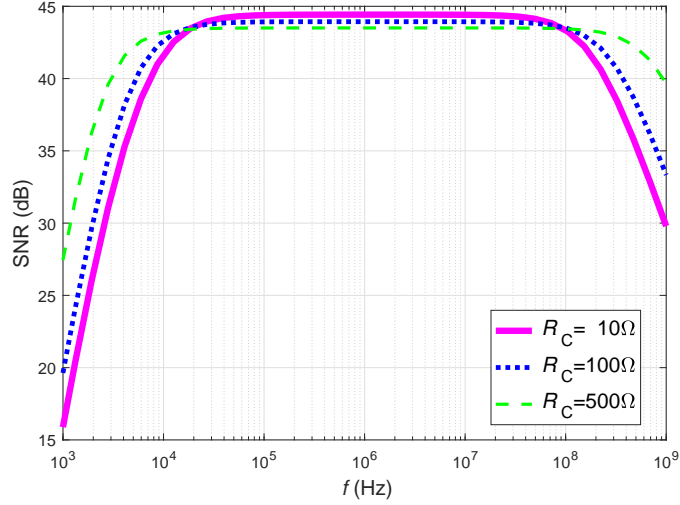


Fig. 12 SNR vs. Carrier Frequency

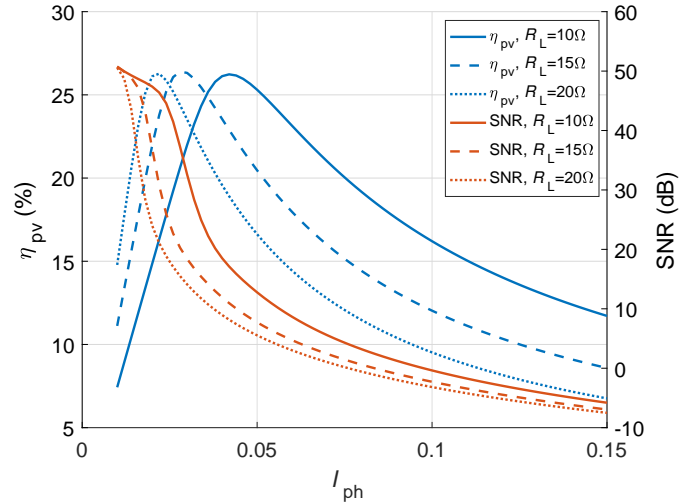


Fig. 13 Trade-off on PV Conversion Efficiency and SNR

efficiency curve is steeper and the high-efficiency region (for example,  $\eta_{\text{pv}} > 20\%$ ) is narrower with the larger deployment of  $R_L$ . From the investigation on Fig. 9, the operating point with large  $I_{\text{ph}}$  lies in the right linear region where the small dynamic resistance and the heavy signal attenuation can be obtained. From the results depicted in Fig. 13, the maximum efficiency point will reaches a low SNR, while high SNR will always cooperate with a low conversion efficiency. We can conclude that it is important to select a proper operating point or operating region for the purpose of an optimal balance between the power conversion efficiency and the SNR.

## V. CONCLUSIONS

We proposed the resonant beam communication (RBCCom) system to realize simultaneous wireless information and power transfer (SWIPT). We at first introduced the structure and the mechanism of the RBCCom system. Then, we

demonstrated the analytical model of the RBCom system to investigate the beam generation, the beam transmission and the energy conversion processes. We also investigated the information modulation, the noises and the signal-to-noise ratio (SNR) at the receiver. Numerical results show that the high SNR can be achieved. The operating point makes significant effects on the linearity of power conversion, the dynamic resistance and the cell capacitance of receiver's PV panel. At last, the maximum power conversion efficiency point and the SNR at this point vary with the operating point which is determined by the load resistance  $R_L$  and the provided photoelectric current  $I_{ph}$ . Therefore, a trade-off should be made between the SNR and the conversion efficiency by the choice of the operating point. In the future, we will improve the completeness of the RBCom model and analyse the performance of the whole information transfer channel.

#### REFERENCES

- [1] Q. Liu, J. Wu, P. Xia, S. Zhao, W. Chen, Y. Yang, and L. Hanzo, "Charging unplugged: Will distributed laser charging for mobile wireless power transfer work?," *IEEE Vehicular Technology Magazine*, vol. 11, pp. 36–45, Dec. 2016.
- [2] K. David and H. Berndt, "6G vision and requirements: Is there any need for beyond 5G?," *IEEE Vehicular Technology Magazine*, vol. 13, pp. 72–80, July 2018.
- [3] J. M. Kahn and J. R. Barry, "Wireless infrared communications," *Proceedings of the IEEE*, vol. 85, pp. 265–298, Feb. 1997.
- [4] Th. Graf, U. Roth, M. Schmid, J.E. Balmer, and H.P. Weber, "Diode-pumped Nd:YAG amplifier for intersatellite optical communication," *Optics Communications*, vol. 152, pp. 302 – 306, July 1998.
- [5] S. Junique, D. Agren, Q. Wang, S. Almqvist, B. Noharet, and J. Y. Andersson, "A modulating retro-reflector for free-space optical communication," *IEEE Photonics Technology Letters*, vol. 18, pp. 85–87, Jan. 2006.
- [6] J. Öhgren, F. Kullander, L. Sjöqvist, K. Wang, Q. Wang, S. Junique, S. Almqvist, and B. Noharet, "A high-speed modulated retro-reflector communication link with a transmissive modulator in a cat's eye optics arrangement," in *Unmanned/Unattended Sensors and Sensor Networks IV*, vol. 6736, p. 673619, International Society for Optics and Photonics, Oct. 2007.
- [7] D. Killinger, "Free space optics for laser communication through the air," *Opt. Photon. News*, vol. 13, pp. 36–42, Oct. 2002.
- [8] T. Komine and M. Nakagawa, "Fundamental analysis for visible-light communication system using LED lights," *IEEE Transactions on Consumer Electronics*, vol. 50, pp. 100–107, Feb. 2004.
- [9] D. Tsonev, H. Chun, S. Rajbhandari, J. J. McKendry, S. Videv, E. Gu, M. Haji, S. Watson, A. E. Kelly, G. Faulkner, *et al.*, "A 3-Gb/s single-LED OFDM-based wireless VLC link using a gallium nitride  $\mu$ LED," *IEEE Photon. Technol. Lett.*, vol. 26, pp. 637–640, Apr. 2014.
- [10] A. Sahai and D. Graham, "Optical wireless power transmission at long wavelengths," in *Space Optical Systems and Applications (ICSOS), 2011 International Conference on*, pp. 164–170, IEEE, May 2011.
- [11] J. Mukherjee, S. Jarvis, M. Perren, and S. J. Sweeney, "Efficiency limits of laser power converters for optical power transfer applications," *Journal of Physics D: Applied Physics*, vol. 46, p. 264006, June 2013.

- [12] S.-M. Kim and S.-M. Kim, "Wireless optical energy transmission using optical beamforming," *Optical Engineering*, vol. 52, p. 043205, Apr. 2013.
- [13] W. Zhou and K. Jin, "Efficiency evaluation of laser diode in different driving modes for wireless power transmission," *IEEE Transactions on Power Electronics*, vol. 30, pp. 6237–6244, Nov. 2015.
- [14] P. K. Sharma, S. Banerjee, S. Bose, B. Jana, O. Goswami, S. Sen, P. Dey, A. Bhunia, P. Modak, A. Shyam, *et al.*, "Performance of vertical multi junction solar cell for long distance wireless power transfer using high intensity laser beam," in *Ubiquitous Computing, Electronics and Mobile Communication Conference (UEMCON), 2017 IEEE 8th Annual*, pp. 553–559, IEEE, Oct. 2017.
- [15] V. Iyer, E. Bayati, R. Nandakumar, A. Majumdar, and S. Gollakota, "Charging a smartphone across a room using lasers," *Proceedings of the ACM on Interactive, Mobile, Wearable and Ubiquitous Technologies*, vol. 1, p. 143, Dec. 2018.
- [16] C. Wu, J. Wang, and C. Huang, "A coupled model on energy conversion in laser power beaming," *Journal of Power Sources*, vol. 393, pp. 211–216, July 2018.
- [17] T. Miyamoto, "Optical wireless power transmission using vcsels," in *Semiconductor Lasers and Laser Dynamics VIII*, vol. 10682, p. 1068204, International Society for Optics and Photonics, May 2018.
- [18] K. Jin and W. Zhou, "Wireless laser power transmission: A review of recent progress," *IEEE Transactions on Power Electronics (Early Access)*, pp. 1–17, July 2018.
- [19] J. Fakidis, S. Kucera, H. Claussen, and H. Haas, "On the design of a free space optical link for small cell backhaul communication and power supply," in *Communication Workshop (ICCW), 2015 IEEE International Conference on*, pp. 1428–1433, IEEE, June 2015.
- [20] H. S. Dhadwal, J. Rastegar, and P. Kwok, "Wireless energy and data transfer to munitions using high power laser diodes," in *Unmanned Systems Technology XIX*, vol. 10195, p. 1019513, International Society for Optics and Photonics, May 2017.
- [21] J. Fakidis, S. Videv, H. Helmers, and H. Haas, "0.5-Gb/s OFDM-based laser data and power transfer using a gaas photovoltaic cell," *IEEE Photonics Technology Letters*, vol. 30, pp. 841–844, May 2018.
- [22] Q. Zhang, W. Fang, Q. Liu, J. Wu, P. Xia, and L. Yang, "Distributed laser charging: A wireless power transfer approach," *IEEE Internet of Things Journal (Early Access)*, pp. 1–1, June 2018.
- [23] Q. Zhang, X. Shi, Q. Liu, J. Wu, P. Xia, and Y. Liao, "Adaptive distributed laser charging for efficient wireless power transfer," in *2017 IEEE 86th Vehicular Technology Conference (VTC-Fall)*, pp. 1–5, Sept. 2017.
- [24] W. Fang, Q. Zhang, Q. Liu, J. Wu, and P. Xia, "Fair scheduling in resonant beam charging for IoT devices," *IEEE Internet of Things Journal (Early Access)*, vol. 1, pp. 1–1, July 2018.
- [25] M. Xiong, M. Liu, Q. Zhang, Q. Liu, J. Wu, and P. Xia, "TDMA in adaptive resonant beam charging for IoT devices," *IEEE Internet of Things Journal (Early Access)*, vol. 1, pp. 1–1, Aug. 2018.
- [26] Z. Wang, D. Tsonev, S. Videv, and H. Haas, "On the design of a solar-panel receiver for optical wireless communications with simultaneous energy harvesting," *IEEE Journal on Selected Areas in Communications*, vol. 33, pp. 1612–1623, Aug 2015.
- [27] J. Liu, *Photonic Devices: Semiconductor lasers and light-emitting diodes*. Cambridge University Press.

- [28] W. Wang, Q. Zhang, H. Lin, M. Liu, X. Liang, and Q. Liu, “Wireless energy transmission channel modeling in resonant beam charging for IoT devices,” *arXiv preprint arXiv:1807.05980*, July 2018.
- [29] Nelson and Jenny, *The physics of solar cells*. Imperial College Press,, 2003.
- [30] D. Sera, R. Teodorescu, and P. Rodriguez, “Pv panel model based on datasheet values,” in *2007 IEEE International Symposium on Industrial Electronics*, pp. 2392–2396, June 2007.
- [31] W. Zhou and K. Jin, “Optimal photovoltaic array configuration under gaussian laser beam condition for wireless power transmission,” *IEEE Transactions on Power Electronics*, vol. 32, pp. 3662–3672, May 2017.
- [32] J. Fakidis, S. Videv, S. Kucera, H. Claussen, and H. Haas, “Indoor optical wireless power transfer to small cells at nighttime,” *Journal of Lightwave Technology*, vol. 34, pp. 3236–3258, July 2016.
- [33] T. L. Grotzinger, “Effects of atmospheric conditions on the performance of free-space infrared communications,” in *Free-Space Laser Communication Technologies III*, vol. 1417, pp. 484–496, International Society for Optics and Photonics, Jun. 1991.
- [34] V. Schlosser and A. Ghitas, “Measurement of silicon solar cells AC parameters,” in *Proceedings of the Arab Regional Solar Energy Conference*, Nov. 2006.
- [35] R. A. Kumar, M. Suresh, and J. Nagaraju, “Measurement and comparison of AC parameters of silicon (BSR and BSFR) and gallium arsenide (GaAs/Ge) solar cells used in space applications,” *Solar energy materials and solar cells*, vol. 60, pp. 155–166, Jan. 2000.
- [36] H. Mandal and J. Nagaraju, “GaAs/Ge and silicon solar cell capacitance measurement using triangular wave method,” *Solar energy materials and solar cells*, vol. 91, pp. 696–700, May 2007.
- [37] M. Deshmukh and J. Nagaraju, “Measurement of silicon and GaAs/Ge solar cells ac parameters,” *Solar Energy*, vol. 78, pp. 1–4, Jan. 2005.
- [38] R. L. Boylestad and L. Nashelsky, *Electronic Devices and Circuit Theory*. Upper Saddle River, NJ, USA: Prentice Hall Press, 10 ed., 2008.
- [39] B. R. Strickland, M. J. Lavan, E. Woodbridge, and V. Chan, “Effects of fog on the bit-error rate of a free-space laser communication system,” *Appl. Opt.*, vol. 38, pp. 424–431, Jan. 1999.
- [40] M. A. Khalighi and M. Uysal, “Survey on free space optical communication: A communication theory perspective,” *IEEE Communications Surveys Tutorials*, vol. 16, pp. 2231–2258, June 2014.
- [41] R. A. Kumar, M. S. Suresh, and J. Nagaraju, “Effect of solar array capacitance on the performance of switching shunt voltage regulator,” *IEEE Transactions on Power Electronics*, vol. 21, pp. 543–548, Mar. 2006.
- [42] S. Rühle, “Tabulated values of the Shockley-Queisser limit for single junction solar cells,” *Solar Energy*, vol. 130, pp. 139–147, June 2016.